buildings

MDPI

Article

Analysis of Factors Affecting the Seismic Performance of Widened Flange Connections in Mid-Flange H-Beams and Box Columns

Tigist Demssice Gemechu and Linfeng Lu *

School of Civil Engineering, Chang'an University, 75 Chang'an Middle Rd, Xi'an 710062, China; 2021028906@chd.edu.cn

* Correspondence: lulinfeng@chd.edu.cn

Abstract: Following the Northridge and Kobe earthquakes, research has increasingly focused on achieving high ductility in beam-to-column connections. This study investigates the seismic performance of connections featuring widened beam-end flanges in mid-flange H-beams and box columns, an area with limited prior research compared to I-section columns and narrow-flange H-beams. Detailed finite element modeling using ABAQUS 6.1.4 demonstrates that widened beam-end flanges significantly improve bending capacity and ductility by relocating the plastic hinge away from the connection, thereby enhancing seismic resilience. Key findings include the identification of optimal design parameters: flange length ranging from 0.55 to 0.75 times the beam flange width, beam flange cutting length between 0.36 and 0.39 times the beam depth, and flange cutting depth from 0.19 to 0.23 times the beam flange width. These parameters ensure effective plastic hinge development and improved structural performance. This study introduces a novel approach that emphasizes geometric optimization over material-based enhancements, offering a cost-effective and practical solution for improving seismic performance and extending previous research insights.

Keywords: steel moment frame; seismic performance; connection; box column; widened beam-end flange

Citation: Gemechu, T.D.; Lu, L. Analysis of Factors Affecting the Seismic Performance of Widened Flange Connections in Mid-Flange H-Beams and Box Columns. *Buildings* **2024**, *14*, 3170. https://doi.org/10.3390/buildings14103170

Academic Editor: Hiroshi Tagawa

Received: 3 September 2024
Revised: 28 September 2024
Accepted: 1 October 2024
Published: 5 October 2024

1. Introduction

As the nation progresses, the push for energy-saving and emission reduction has driven the move away from traditional building materials high in energy consumption and pollution. Steel structures, with their lightweight, strong, seismically resilient, highly industrialized, and environmentally friendly advantages, are anticipated to become mainstream in the construction industry [1]. The beam–column connection, vital to a steel frame's seismic performance, must effectively balance deformation and energy dissipation. Design principles emphasize "strong columns, weak beams" and "strong joints, weak members". In China's steel frames, rigid connections, including bolt, weld, and hybrid types, are commonly used [2]. However, the brittle failure of traditional welded joints during the Northridge (1994) and Kobe (1995) earthquakes has led to a shift toward high-ductility connections [3]. Researchers have since focused on enhancing beam–column connections by either reinforcing the beam end to shift the plastic hinge away from the joint or weakening the beam to ensure plastic deformation occurs before the beam ends, thus improving ductility and preventing brittle failure [4]. Developing high-ductility beam–column connections has become a critical area of study [5].

Recent studies emphasized the importance of joint ductility in steel frames for better seismic performance. Han et al. [6] analyzed the behavior of steel frames under cyclic loads and developed a high-performance joint design that enhances energy dissipation. Their findings align with earlier studies and further highlight the need for improved ductility in beam–column connections to mitigate the impact of seismic forces.

Yang et al. [7] also conducted an experimental investigation into the cyclic performance of UHPSFRC-filled thin-walled steel tubular columns subjected to combined axial compression and cyclic lateral displacement loading. Their study meticulously analyzed failure modes, hysteretic behaviors, and energy dissipation capacities. The research revealed that UHPSFRC significantly enhances the cyclic behavior of thin-walled steel tubular columns compared to high-strength concrete (HSC) and normal-strength concrete (NSC). Notably, UHPSFRC-filled columns demonstrated superior ductility, stiffness, and energy dissipation, making them more resilient to seismic activities. The investigation also highlighted the influence of various design parameters, such as steel tube thickness and steel fiber volume ratio, on the seismic performance of these columns.

Further enhancing this understanding, a study by Wei et al. [8] focused on concrete-filled steel tubular (CFST) composite columns with ultra-high-performance concrete (UHPC) plates. Their research revealed that UHPC improved the specimen's initial stiffness by 13.7% and increased hysteretic energy dissipation by 41.2%. Additionally, the specimens demonstrated excellent seismic performance, even under mainshock–aftershock sequences, indicating the structure's ability to withstand multiple earthquakes. This highlights the critical role of innovative materials in enhancing the seismic performance of steel and composite structures.

Two main types of improved connections have been proposed to shift the plastic hinge outward, as illustrated in Figure 1. The first type is the beam-end reinforced connection, designed to increase joint stiffness. By enhancing the bending stiffness at the beam–column connection, the beam flange can plastically deform away from the column flange surface, forming a plastic hinge that reduces stress concentration at the beam–column groove weld. The second type, shown in Figure 2, is a weakened connection. This approach aims to induce plastic deformation in the weakened part of the beam before the beam ends, enhancing joint ductility and protecting the joint from brittle failure.

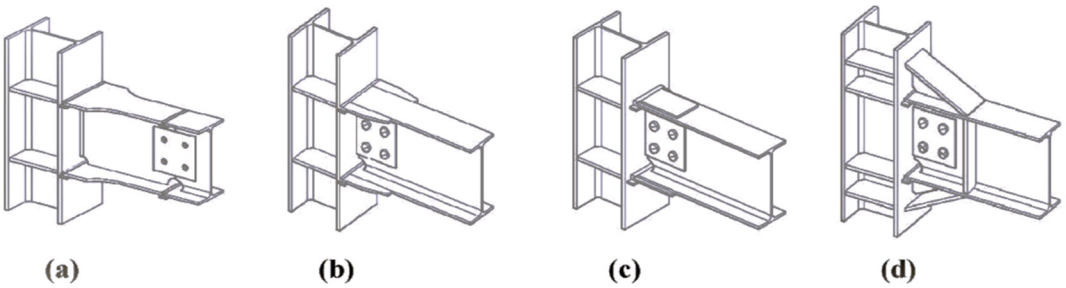

Figure 1. Enhanced connections. (**a**) Widened flange; (**b**) Side plate reinforced; (**c**) Cover reinforced; (**d**) Haunch reinforcement.

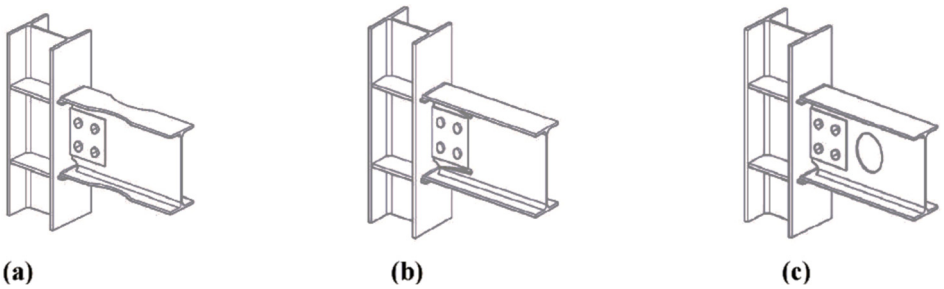

Figure 2. Weakened connections. (**a**) RBS; (**b**) Beam web slit; (**c**) Beam web opening.

Various studies have explored the seismic performance of beam–column connections with expanded beam flanges. Wang [9] found that flange expansion in large-scale joints significantly reduces stress concentration and meets FEMA standards. Nia et al. [10] showed that joints with expanded flanges and shear cover plates improve seismic performance, achieving a plastic angle of 0.06 rad. Lu et al. [11] emphasized the importance of weld

quality in hybrid connections. Ma et al. [12] tested the impact of flange size on cyclic behavior, finding that while flange expansion slightly affects stiffness and energy dissipation, it influences plastic hinge positioning. Wang [13] further analyzed the effects of beam flange widening, concluding that appropriate weakening and flange size adjustments enhance seismic performance, although excessive widening yields diminishing returns.

Recent research further advanced the understanding of beam–column connections. Zohdi et al. [14] investigated the seismic performance of enlarged beam section connections, highlighting joint design and performance improvements. Xiao et al. [15] conducted finite element analysis on prefabricated semi-rigid concrete beam–column joints with steel connections, providing new insights into their behavior under seismic loads. Han et al. [6] explored the seismic behavior of high-performance steel weakened beam–column joints through experimental tests and numerical analysis, offering valuable data on the effectiveness of various connection designs.

Despite extensive research on the seismic performance of beam–column connections with I-section columns and narrow-flange H-beams, the behavior of mid-flange H-beams, which are increasingly used in modern engineering, remains underexplored. The unique characteristics of widened beam-end flanges in mid-flange H-beams and box columns, particularly their influence on plastic hinge formation and stress distribution, require further investigation. While the outward shift of the plastic hinge reduces weld stress, it introduces new challenges, such as increased deformation in the beam web and potential local buckling. This study addresses these gaps by conducting detailed finite element simulations to evaluate the seismic performance of these connections. The findings will provide insights into improving connection design and enhancing steel structure stability and resilience in modern construction practices.

2. Design Specification for Widened Flange Connection

This study examines the expanded flange joint with a weld-bolt hybrid connection, as shown in Figure 3.

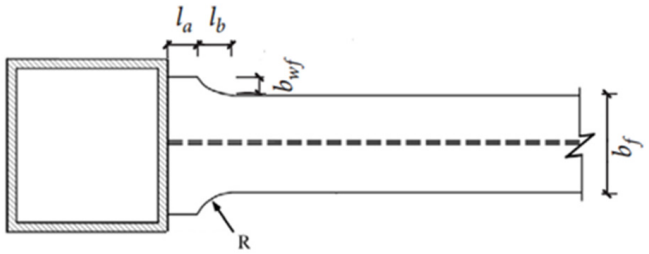

Figure 3. Shapes and sizes of beam.

A widened beam flange connection was proposed to shift the plastic hinge on the beam away from the column [16]. In this design, the beam flanges are enlarged at the beam ends near the column, reinforcing the beam-to-column connection. This reinforcement aims to increase the beam's flexural capacity at the interface, as illustrated in Figure 3. With the widened beam flange at the joint, the plastic hinge is expected to form on the beam section beyond the widened flange. When the auxiliary expansion type connects the flange at the beam's end, the length of the added auxiliary section should follow these dimensions: l_a = 0.50–0.75 b_f, l_b = 0.30–0.45 h_b, and b_{wf} = 0.15–0.25 b_f, where l_a and l_b are the widened flange length, beam flange cutting length, and b_{wf} is the cutting depth of the widened flange [17]:

$$R = \frac{l_b^2 + b_{wf}^2}{2b_{wf}} \quad (1)$$

3. Numerical Analysis Methods

3.1. Numerical Modeling

To fully account for the effects of boundary conditions and joint performance on the upper and lower columns and beam ends, this simulation uses an external-column joint in a steel frame between beam–column inflection points under horizontal load. Typically, a column's inflection point is located at its midpoint under horizontal load, while a beam's inflection point depends on the load position and geometry of the column and beam. For a horizontal load, the reverse bending point is at mid-span; for a vertical load, it is approximately 1/3 to 1/4 of the span from the beam end. This study's beam and column dimensions are 3000 mm and 3600 mm (measured from the hinge center).

The ABAQUS finite element analysis technology is mature and reliable. In this analysis, the beam–column connection is expected to deform locally. To improve accuracy, the C3D8I element was chosen for its ability to handle shear locking and contact-heavy models, requiring minimal elements for bending analysis. The mesh is refined at critical areas like plastic hinges and contact points, while a coarser mesh is used at distant locations to save computation time, as shown in Figure 4. Sweep meshing is applied to screw holes, and structured meshing is used elsewhere to maintain mesh quality.

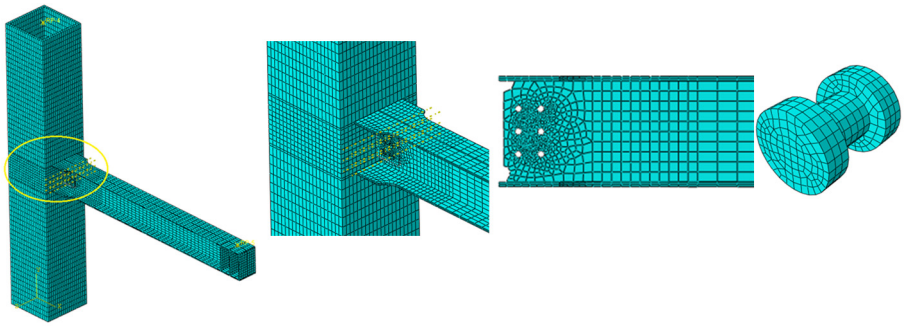

(**a**) (**b**) (**c**)

Figure 4. Mesh of a specimen. (**a**) Overall mesh of a specimen and joint; (**b**) Mesh of screw holes and beam; (**c**) Mesh of a bolt.

Contact is nonlinear, making analysis and convergence challenging. With pre-tension applied to high-strength bolts, various contact relationships form. To simplify modeling, bolts are represented with circular heads, smooth surfaces, and no threads. Key contacts include plate-to-beam web, bolt head-to-web, and screw-to-hole wall, simulated using the ABAQUS "surface-to-surface" method. The higher stiffness surface is the master, and the lower is the slave. Normal contact is defined as "hard", with surfaces touching under pressure and separating otherwise, while tangential contact is modeled as "Coulomb friction", using the actual anti-slip coefficient 0.44 [18] of the friction surface of the bolt connection. The design pre-tension value is given according to JGJ82-2010 [19], and the "bolt load" of ABAQUS is used to simulate. The "TIE" command to simulate the welding; the local schematic diagram of contact and binding constraints of the finite element model is shown in Figure 5. Reference coupling points are placed at the top, bottom, and beam end. The column bottom restricts all translational movement, the column top restricts out-of-plane movement, and the beam end restricts out-of-plane and vertical movement. Lateral support is simulated by restricting out-of-plane movement at the beam flange. Vertical axial force and horizontal cyclic displacement are applied to the column top.

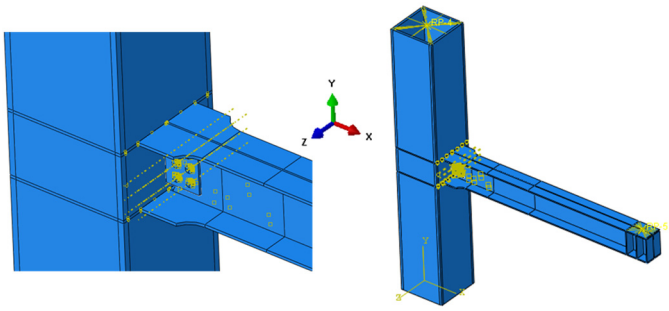

(**a**) (**b**)

Figure 5. Constraints and boundary conditions. (**a**) Contact and binding constraints; (**b**) Boundary conditions.

3.2. Material Property Assumptions and Parameters

As shown in Figure 6, assuming the steel and bolt materials follow a three-line isotropic hardening model with a corresponding stress–strain curve, σ_y, σ_u, and σ_{st} represent the yield, maximum, and failure stresses, while ε_y, ε_u, and ε_{st} are the associated strains. Q235 steel's properties are averaged from the stress–strain data of Nie et al. [20] and 8.8 grade M20 bolt properties based on Kontolati et al. [21], as listed in Table 1.

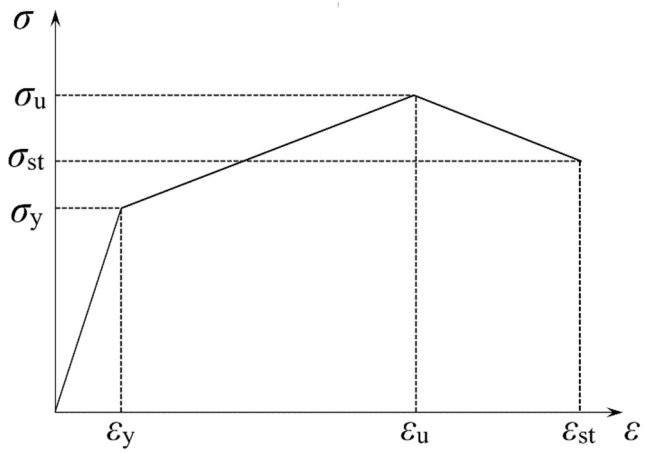

Figure 6. Three-line stress–strain relationship curve.

Table 1. Material properties of Q235 steel and 8.8 grade bolt.

Material Samples	*E*/MPa	σ_y/MPa	ε_y	σ_u/MPa	ε_u	σ_{st}/MPa	ε_{st}
Q235 steel	197,000	320	0.01748	451.667	0.14361	360.643	0.19653
8.8 grade M20 bolt	161,000	645.0	0.004	793.5	0.025	636.9	0.121

3.3. Validation

The SPS-2 specimen by Gao [22] is selected with specific dimensions, and the finite element model is shown in Figure 7. The beam and column specimens were selected as hot-rolled steel sections HN300 × 150 × 6.5 × 9 and HW250 × 250 × 9 × 14, respectively. The steel material is Q235, with a measured yield strength of 299.2 MPa and tensile strength of 420.6 MPa. The specimen loading protocol followed ANSI/AISC 341-05 [23], with six cycles at inter-story drift angles of 0.375% rad, 0.5% rad, 0.75% rad, and four cycles at 1% rad. For drift angles of 1.5% rad, 2% rad, 3% rad, and 4% rad, two cycles were applied for each. Afterwards, for every additional 1% rad, two cycles are applied. Loading was stopped when the bearing capacity dropped to 85% of the maximum load. Following the test loading protocol, displacement-controlled cyclic loading is applied at the beam end [22].

During the test, the column top force is 850 kN (the corresponding axial compression ratio is 0.4), the bolt pre-tension is 155 kN, and the friction coefficient between the connection plate, web, and bolts is 0.35.

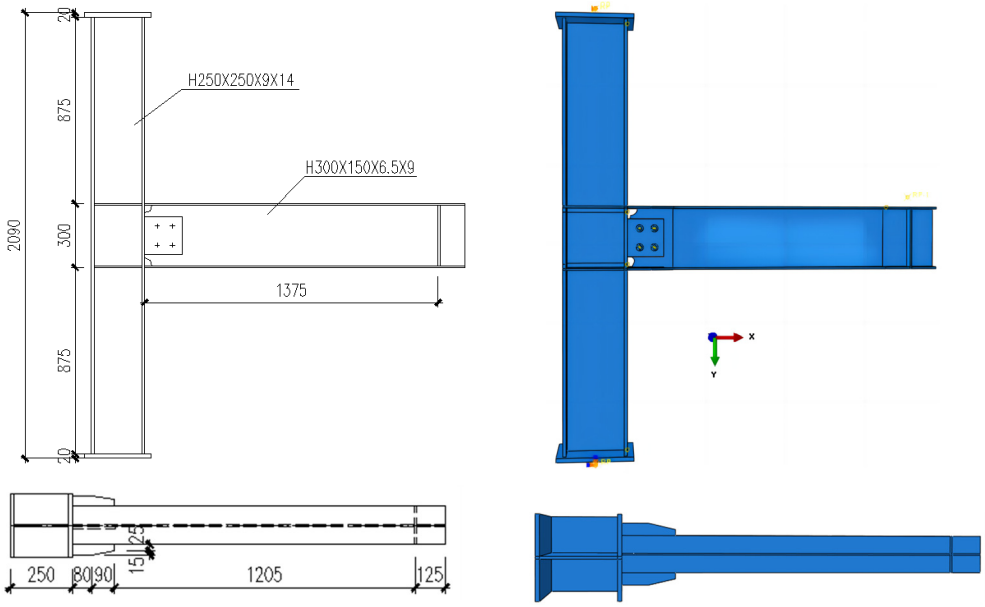

(**a**) (**b**)

Figure 7. SPS-2 Specimen. (**a**) Schematic diagram of dimensions; (**b**) FE Model.

The P–Δ hysteresis curve obtained from the experiment for the SPS-2 specimen is shown in Figure 8a, while the P–Δ hysteresis curve obtained from the finite element analysis is shown in Figure 8b. The failure modes of the SPS-2 specimen from the experiment and the finite element analysis are shown in Figures 9a and 9b, respectively.

The failure modes of the SPS-2 specimen from the experiment and the finite element model are generally consistent. Although there are some differences between the experimental and finite element hysteresis curves, their shapes are similar, showing a spindle shape with near-symmetry and no significant pinching. The maximum load obtained from the finite element model was 164.23 kN, while the experimental maximum load was 158.97 kN, with a 3.3% error. This indicates that the numerical analysis method used in this study is highly reliable.

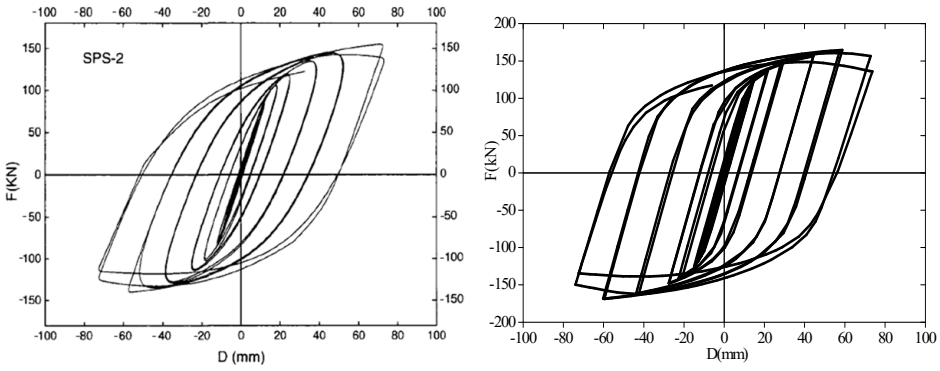

(**a**) (**b**)

Figure 8. P–Δ curves of SPS-2 Specimen. (**a**) Test; (**b**) ABAQUS.

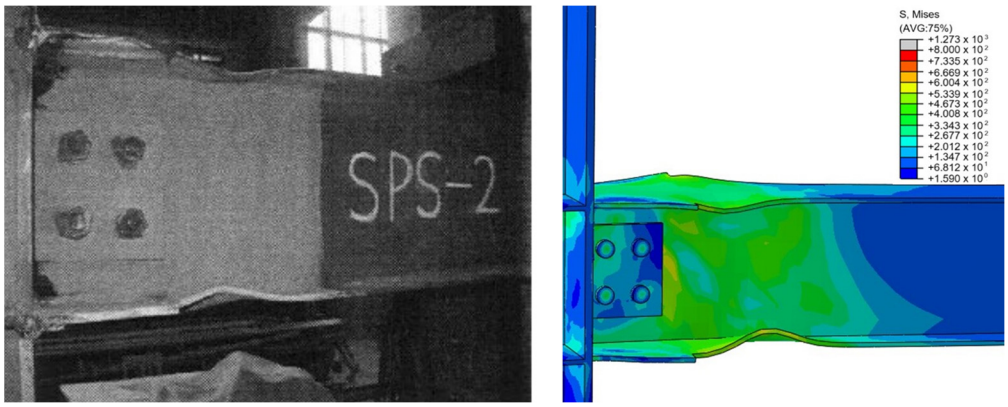

(**a**) (**b**)

Figure 9. Failure modes of SPS-2 Specimen. (**a**) Test; (**b**) ABAQUS.

4. Design of Analysis Specimens

Three key design parameters were investigated for the widened flange connection: l_a, l_b, and b_{wf}. Three series were analyzed: WFS-250A, WFS-250B, and WFS-250C. Six joint configurations were modeled for each series for finite element analysis (see Table 2, and R is calculated by Equation (1)). A connection with no widened flange is termed "UW" for comparison. The column was box-section 500 × 500 × 16, and the H-shape beam was HM340 × 250 × 9 × 14. The steel was grade 235, and the material property data were in reference [11]. The parameters all met design specification JGJ99-2015 [17].

Table 2. Properties of WFS-250 specimens.

Specimens			l_a/mm	l_a/b_f	l_b/mm	l_b/h_b	b_{wf}/mm	b_{wf}/b_f	R/mm
WFS-250	A	A-1	125	0.50	102	0.30	62.5	0.25	114.5
		A-2	137.5	0.55	102	0.30	62.5	0.25	114.5
		A-3	150	0.60	102	0.30	62.5	0.25	114.5
		A-4	162.5	0.65	102	0.30	62.5	0.25	114.5
		A-5	175	0.70	102	0.30	62.5	0.25	114.5
		A-6	187.5	0.75	102	0.30	62.5	0.25	114.5
	B	B-1	125	0.50	102	0.30	62.5	0.25	114.5
		B-2	125	0.50	112.2	0.33	62.5	0.25	132.0
		B-3	125	0.50	122.4	0.36	62.5	0.25	151.1
		B-4	125	0.50	132.6	0.39	62.5	0.25	171.9
		B-5	125	0.50	142.8	0.42	62.5	0.25	194.4
		B-6	125	0.50	153	0.45	62.5	0.25	218.5
	C	C-1	125	0.50	102	0.30	37.5	0.15	157.5
		C-2	125	0.50	102	0.30	42.5	0.17	143.7
		C-3	125	0.50	102	0.30	47.5	0.19	133.3
		C-4	125	0.50	102	0.30	52.5	0.21	125.3
		C-5	125	0.50	102	0.30	57.5	0.23	119.2
		C-6	125	0.50	102	0.30	62.5	0.25	114.5

5. Analysis Results and Discussing

5.1. WFS-250-A Series Joints

5.1.1. Joint Failure Mode

Figure 10 shows the PEEQ cloud diagram for the WFS-250-A series joints at failure. Figure 11 presents the curve of the maximum PEEQ value at the plastic hinge of WFS-250-A series joints as a function of loading displacement.

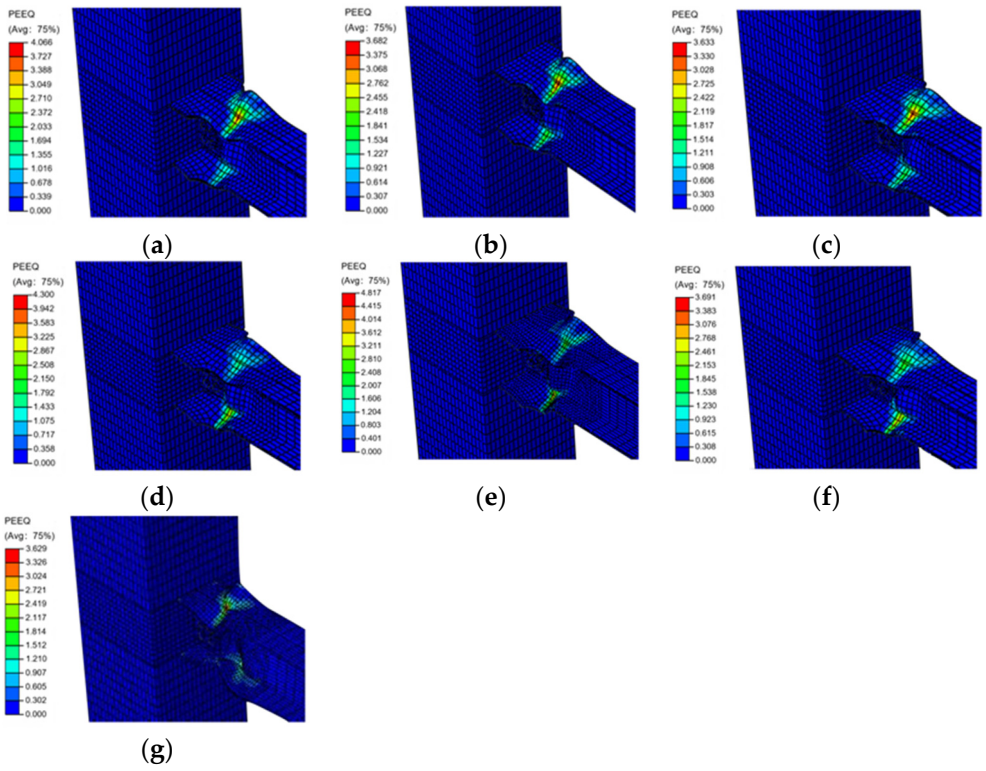

Figure 10. PEEQ cloud chart of WFS-250-A series joints at failure time. (**a**) WFS-250-A-1; (**b**) WFS-250-A-2; (**c**) WFS-250-A-3; (**d**) WFS-250-A-4; (**e**) WFS-250-A-5; (**f**) WFS-250-A-6; (**g**) UW-250.

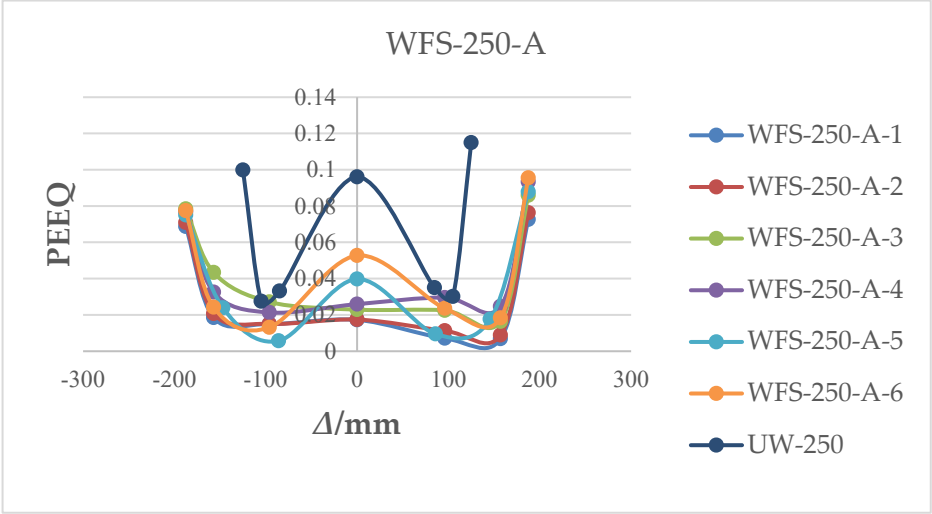

Figure 11. PEEQ maximum at the plastic hinge of WFS-250-A series and UW-250 joints.

Figure 10 shows that the equivalent plastic deformation distribution for the WFS-250-A series joints is uniform at failure. The upper and lower beam flanges expand and deform at the widened sections and their ends, forming distinct plastic hinges. As the reinforced section l_a length increases, the plastic hinge moves outward, while the PEEQ value at the beam-to-column flange joint decreases, indicating reduced cumulative plastic deformation in the weld. The maximum PEEQ value is found on the beam web where the weld passes through, suggesting a reduced risk of brittle fracture in the weld and achieving the goal of weld protection [24,25]. The joint domain remains intact, with the column flange largely elastic and with minimal deformation, demonstrating a "strong joint" characteristic.

In the WFS-250-A series, the failure is predominantly influenced by the plastic deformation in the widened beam flanges. High levels of equivalent plastic strain (PEEQ) are observed at the ends of the reinforced sections, leading to local buckling of the flanges. This buckling is initiated due to the cyclic nature of seismic loading, where plastic deformation progressively accumulates.

A plastic hinge forms near the ends of the widened flange sections, which helps reduce stress concentration at the weld between the beam and column flanges. The outward shift of the plastic hinge protects the weld from brittle fracture. However, the widening of the flanges, while effective in energy dissipation, creates instability in these regions, causing flange buckling. This buckling, in turn, undermines the overall integrity of the joint, leading to failure.

The key reason for the failure in the WFS-250-A series is the inability of the widened flange sections to sustain plastic deformation without local instability. As the flanges buckle, the joint loses its capacity to continue absorbing seismic energy, resulting in structural failure.

Figure 11 shows the peak PEEQ values observed at the extreme edges of the beam flange groove weld. When the widened flange was used in WFS-250-A-6, the maximum PEEQ decreased by 16.9% (from 0.115 rad to 0.095 rad) and by 36.9% for WFS-250-A-1 (from 0.115 rad to 0.073 rad) compared to UW-250. A wider flange at the beam–column interface results in a lower PEEQ index. The WFS-250-A-6 joint showed the highest maximum PEEQ, indicating the most accumulated plastic deformation at the plastic hinge, while WFS-250-A-1 had the least. As the length l_a increased, the outward displacement of the plastic hinge decreased, and the maximum PEEQ value first was reduced and then increased, reflecting a similar trend in the cumulative plastic deformation at the plastic hinge.

5.1.2. M–θ Hysteresis Curve and Skeleton Curve

Figure 12 shows the moment-angle M–θ hysteretic and skeleton curves for the WFS-250-A series joints. In Figure 12a, the M–θ hysteretic curves for all joints display a similar, full shuttle shape. With a transition section length l_b of 102 mm and a reinforced section width b_{wf} of 62.5 mm, the seismic performance of the WFS-250-A joints is favorable when l_a is 0.50–0.75 times the beam width. At an inter-story displacement angle of 0.06 rad, the corresponding bending capacity exceeds 0.85 M_p (the plastic moment of the H beam).

Additionally, the M–θ hysteresis curve (Figure 12a) demonstrates the cyclic response of the connection, highlighting its ability to dissipate energy under repeated loading conditions. *X*-axis (Rotation, θ): the horizontal axis represents rotation (θ) in radians, ranging from −0.1 to +0.1 radians. *Y*-axis (Moment, M): the vertical axis represents moment (M) in kNm, with values ranging from −600 kNm to +600 kNm.

The shape of the hysteresis loop illustrates the connection's energy dissipation and ductility under cyclic lateral loads. The broad and stable loops indicate excellent energy absorption with minimal stiffness degradation or slippage. The curves for WFS-250-A-1, WFS-250-A-2, and others show consistency across tests, indicating strong repeatability and reliability of the seismic performance of the connections.

The lack of significant pinching further suggests the connection retains its stiffness, providing robust resistance to seismic forces. The gradual, consistent spread of the loops confirms good ductility, a critical factor in seismic design, allowing the connection to accommodate large rotations without a notable loss of strength.

In Figure 12b, the skeleton curves for all six joints nearly coincide during the elastic stage, where the bending moment and rotation angle increase linearly. As the joints enter the elastic–plastic stage, the curves begin to diverge. The moment at the beam end increases with the length l_a of the reinforced section, placing the WFS-250-A-6 joint skeleton curve on the outermost side. After reaching the peak moment, the skeleton curve shows a decline, with the rate of decline increasing as l_a lengthens, indicating that a longer expanded flange accelerates the reduction in joint bearing capacity.

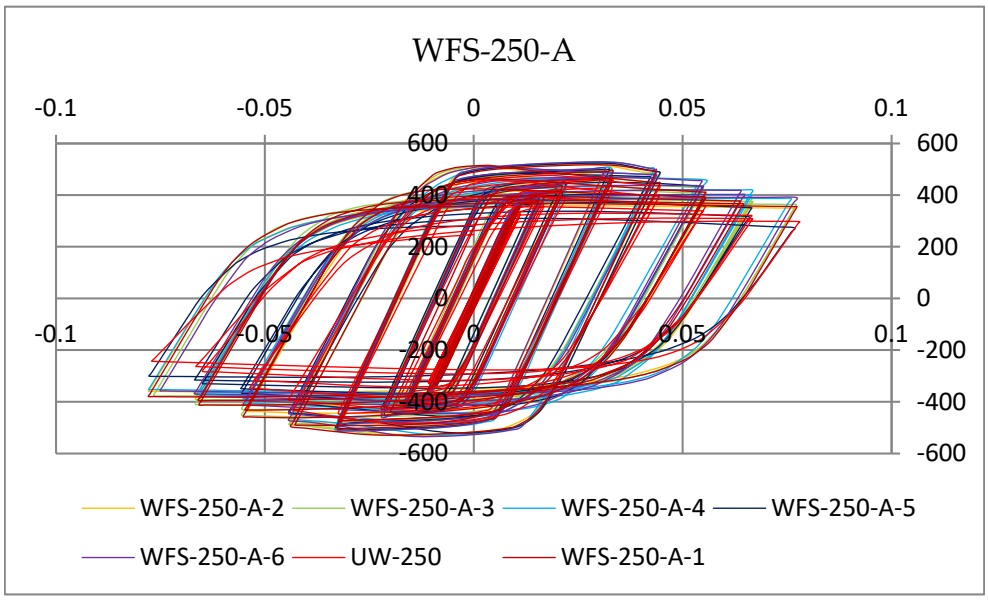

(**a**)

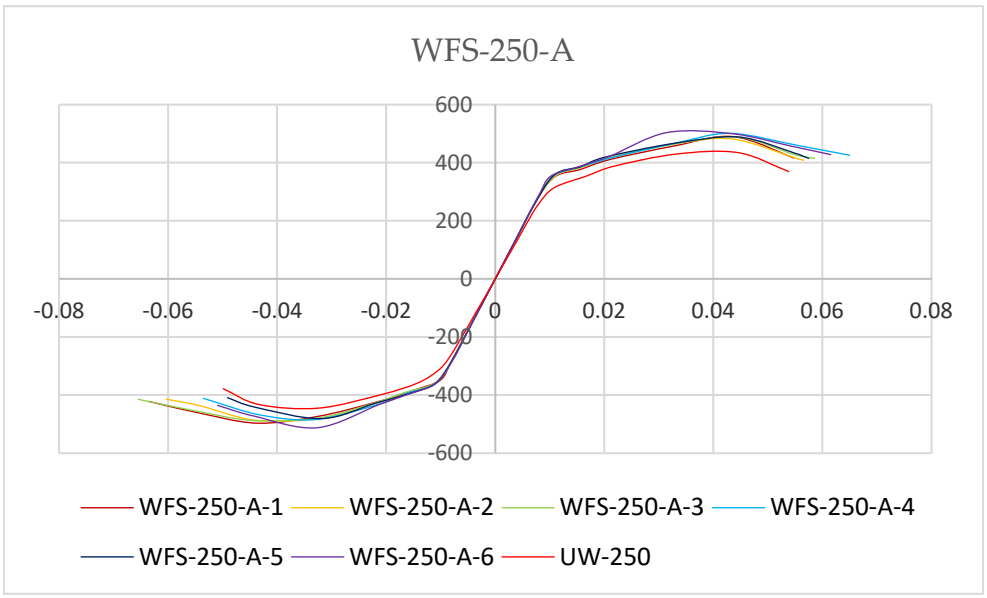

(**b**)

Figure 12. M–θ hysteretic and skeleton curve of WFS-250-A series joints. (**a**) Hysteretic curves; (**b**) Skeleton curves.

The skeleton curve (Figure 12b) is constructed by connecting the peaks of the hysteresis loops, capturing the envelope of the maximum moments achieved at various rotation levels. *X*-axis (Rotation, θ): Rotation values range from −0.08 to +0.08 radians. *Y*-axis (Moment, M): Moment values range from −600 kN·m to +600 kN·m.

The skeleton curve represents the connection's strength and stiffness throughout the loading process. Initially, the connection displays linear elastic behavior, with the moment increasing proportionally to the rotation up to approximately ±0.02 radians. Beyond this point, yielding occurs, indicated by the curve flattening, which signifies plastic deformation. After the maximum moment was reached, a slight reduction in stiffness was observed, signaling some degradation due to cyclic loading.

According to the skeleton curves of the WFS-250-A joint in Figure 12b and the calculation method in reference [11], the joint's mechanical property index under pushing load is

summarized in Table 3. R_{ki} is the initial rotation stiffness. M_y, M_{max}, and M_u are the yield, peak, and ultimate moments, and θ_y, θ_{max}, and θ_u correspond to the rotation displacement.

Table 3. Mechanical performance indexes of WFS-250-A series joints.

Joint Number	R_{ki} /kN·m·rad^{-1}	M_y /kN·m	θ_y /rad	M_{max} /kN·m	θ_{max} /rad	M_u /kN·m	θ_u /rad	θ_p /rad	μ
WFS-250-A-1	35,768.45	389	0.017	489.741	0.044	416.28	0.055	0.037	3.163
WFS-250-A-2	35,882.74	382	0.015	481.171	0.044	409.00	0.056	0.041	3.649
WFS-250-A-3	35,991.44	388	0.016	488.030	0.044	414.83	0.058	0.042	3.661
WFS-250-A-4	36,107.55	399	0.017	500.944	0.043	425.80	0.065	0.047	3.694
WFS-250-A-5	35,951.63	385	0.015	488.460	0.045	415.20	0.057	0.042	3.755
WFS-250-A-6	36,316.66	409	0.019	503.702	0.031	428.15	0.061	0.042	3.237
UW-250	33,086.98	356	0.017	434.696	0.044	369.49	0.054	0.036	3.167

θ_p is the rotation capacity according to FEMA 350 [26]. μ is the ductility factor, $\mu = \theta_u/\theta_y$.

From Table 3, increasing l_a strengthens the expanded flange at the beam end, slightly raising joint rotational stiffness by up to 1.5%. However, this increase in stiffness weakens rotational capacity, with yield and ultimate angles differing by 19.5% and 15.8%, respectively. The yield and maximum bending moments initially decrease and then increase, with maximum increases of 6.6% and 4.5%. The angle ductility shows minimal change, following an initial rise and then a decrease.

By comparing the performance indices of the UW-250 specimen, it is evident that when l_a/b_f is between 0.55 and 0.75 (the corresponding specimens WFS-250-A-2 to WFS-250-A-6.), the joint exhibits excellent plastic rotation capacity and seismic performance.

5.2. WFS-250-B Series Joints

5.2.1. Joint Failure Mode

Figure 13 illustrates the PEEQ distribution for WFS-250-B series joints at failure. Figure 14 shows the curve of the maximum PEEQ at the plastic hinge versus loading displacement for the same series.

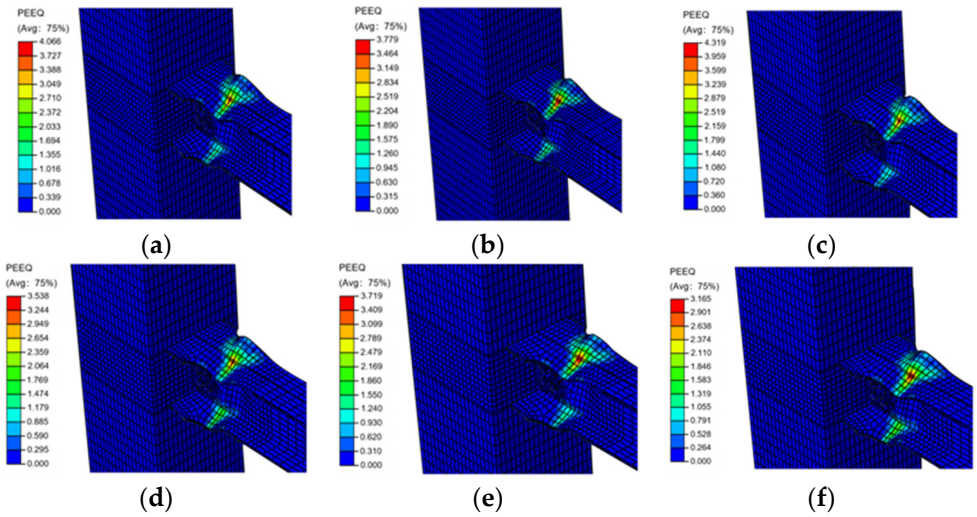

Figure 13. PEEQ cloud chart of WFS-250-B series joints at failure time. (**a**) WFS-250-B-1; (**b**) WFS-250-B-2; (**c**) WFS-250-B-3; (**d**) WFS-250-B-4; (**e**) WFS-250-B-5; (**f**) WFS-250-B-6.

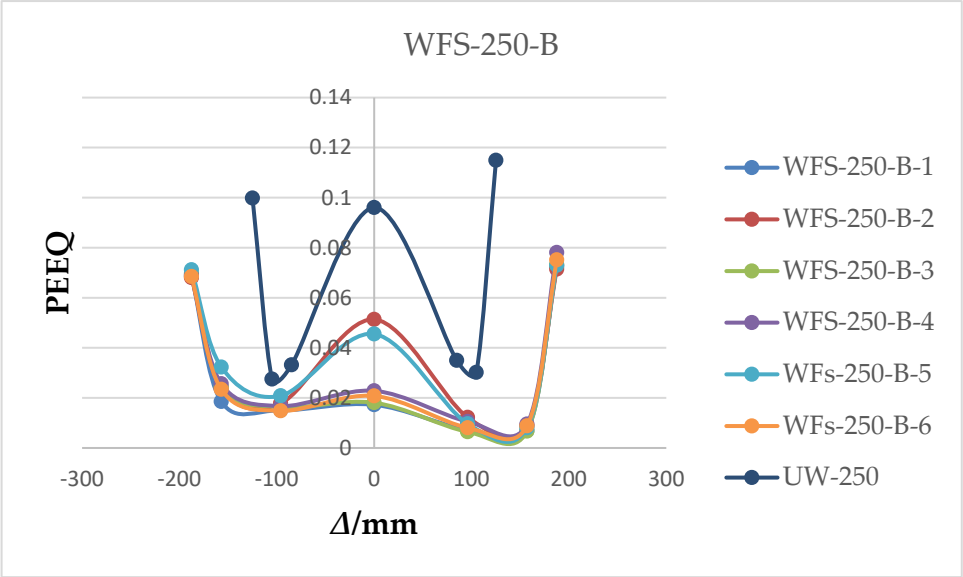

Figure 14. PEEQ maximum at the plastic hinge of WFS-250-B series and UW-250 joints.

As shown in Figures 10 and 13, the WFS-250-B and WFS-250-A series joints exhibit similar failure modes. The upper and lower flanges of the beam show significant buckling deformation, and a plastic hinge forms at the end of the expanded flange. As the length l_b increases, the PEEQ value at the weld between the beam and column flanges gradually decreases, causing the plastic deformation zone to move away from the beam end. The equivalent plastic strain in the beam web outside the connecting plate significantly increases, and the plastic hinge gradually shifts outward. The column flange and joint area experience minimal overall plastic deformation, maintaining their shape and exhibiting the clear characteristics of a "strong joint".

In the WFS-250-B series, the longer transition section (l_b) between the widened flange and the regular beam geometry plays a critical role in the failure mechanism. This longer transition length shifts the plastic hinge further from the beam–column weld, thus reducing the likelihood of weld failure due to brittle fracture. However, this design feature introduces new vulnerabilities.

The outward movement of the plastic hinge leads to increased plastic deformation in the beam web, making it the next critical region of concern. This concentration of deformation in the web may eventually compromise the overall performance of the connection, as the web experiences higher stress levels and potential instability under cyclic loading conditions. As the plastic strain accumulates in the web, it becomes susceptible to significant deformation and eventual buckling. The interaction between the beam flanges and the web, combined with the cyclic nature of seismic loading, leads to the progressive weakening of the web, eventually compromising the joint's integrity.

Thus, while the WFS-250-B series mitigates the risk of weld failure, the plastic strain concentration in the beam web is a significant cause of failure. The beam web's inability to withstand this accumulated deformation ultimately leads to joint failure.

Figure 14 shows that for model UW-250, peak PEEQ values were observed at the extreme edges of the beam flange groove weld. When a widened flange was used, the maximum PEEQ index decreased by 32% for WFS-250-B-4 (from 0.115 to 0.078) and 37.8% for WFS-250-B-2 (from 0.115 to 0.071) compared to UW-250. A wider flange at the beam–column interface reduces the PEEQ index. Figure 13 shows that WFS-250-B-4 has the highest maximum PEEQ at the plastic hinge, indicating the greatest accumulated plastic deformation, while WFS-250-B-2 has the least.

5.2.2. M–θ Hysteresis Curve and Skeleton Curve

Figure 15 shows the moment-angle M–θ hysteretic and skeleton curves for the WFS-250-B series joints. Figure 15a shows that the moment-angle M–θ hysteretic curves for the WFS-250-B series joints are consistently full shuttle-shaped, exhibiting bearing capacity and energy dissipation. When the inter-story drift angle reaches 0.06 rad, the corresponding bending capacity exceeds 0.85 Mp. This indicates that with a reinforced section length l_a of 125 mm and width b_{wf} of 62.5 mm, increasing the transition section length l_b from 0.3 to 0.45 times, the beam depth maintains good seismic performance, similar to WFS-250-A series joints.

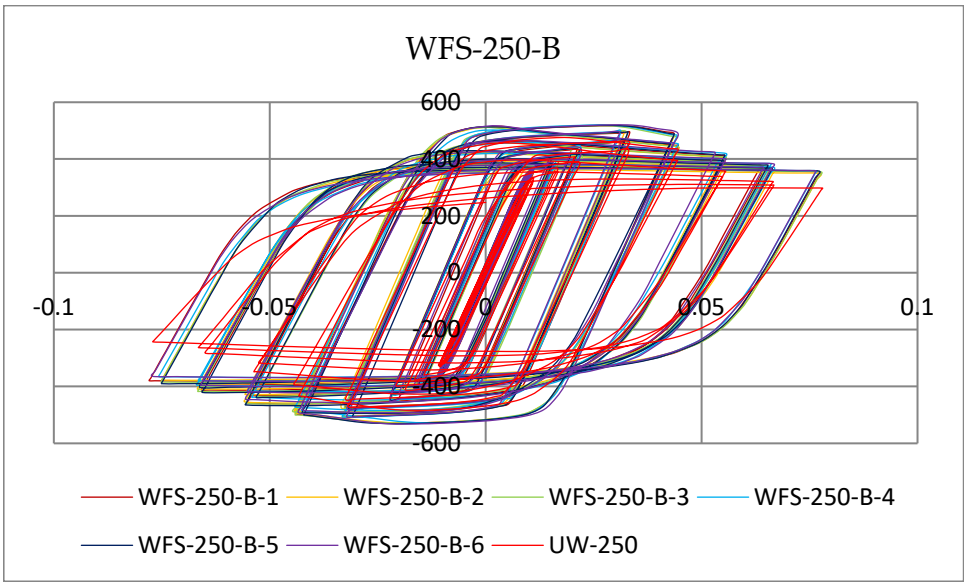

(**a**)

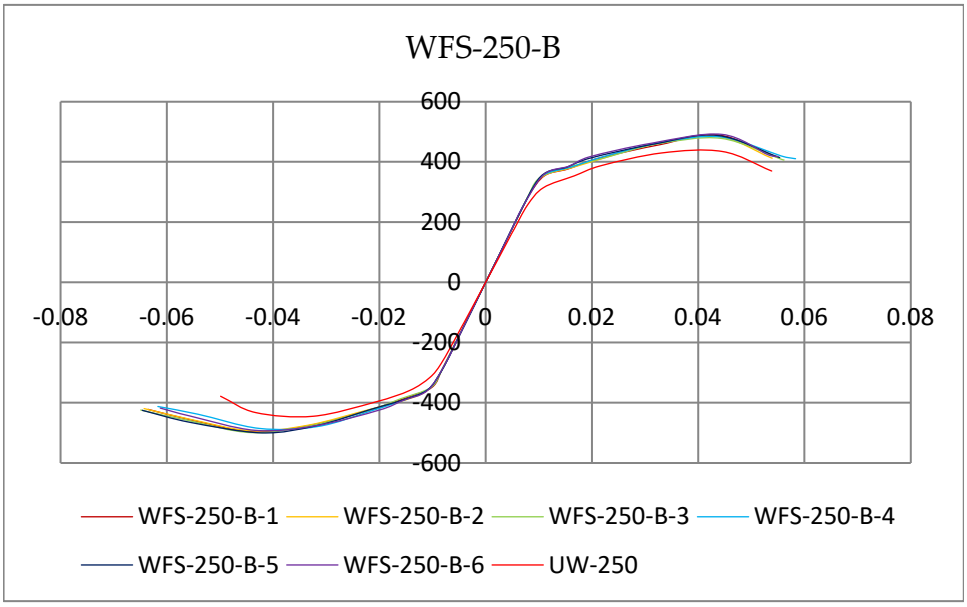

(**b**)

Figure 15. M–θ hysteretic and skeleton curve of WFS-250-B series joints. (**a**) Hysteretic curves; (**b**) Skeleton curves.

The M–θ hysteresis curves for the WFS-250-B series joints, shown in Figure 15a, display the cyclic response of the connections under repeated loading, highlighting their energy dissipation, ductility, and stiffness degradation. The *X*-axis represents rotation

(θ) in radians, ranging from −0.1 to +0.1, while the *Y*-axis represents the moment (M) in kNm, ranging from −600 kNm to +600 kNm. The broad loops indicate significant energy dissipation, essential for seismic performance, while the stable shape of the curves demonstrates good ductility, allowing for large rotations without significant stiffness loss. Minimal pinching in the curves suggests the connections maintain their stiffness well during cyclic loading. Although slight stiffness degradation is observed with increasing cycles, it occurs slowly, indicating strong post-yield performance. The consistent behavior across different specimens (WFS-250-B-1–WFS-250-B-6) confirms the repeatability and reliability of these connections for seismic applications.

The skeleton curve in Figure 15b reveals that all six joints show a similar trend during displacement loading, with bending capacity increasing as l_b increases, and the skeleton curve of WFS-250-B-6 being the outermost. Based on the skeleton curve, Table 4 presents the mechanical performance indices of WFS-250-B series joints. As l_b increases, the initial rotational stiffness and flexural capacity also gradually increase, with maximum increases of 0.7% in initial stiffness and 4.5% in yield moment, while the maximum difference in bending capacity is 2.7%. The yield angle changes by 13%, and the ultimate angle decreases, with a maximum reduction of 7.6%. Angle ductility initially increases and then decreases as bending stiffness increases.

Table 4. Mechanical performance indexes of WFS-250-B series joints.

Joint Number	R_{ki} /kN·m·rad^{-1}	M_y /kN·m	θ_y /rad	M_{max} /kN·m	θ_{max} /rad	M_u /kN·m	θ_u /rad	θ_p /rad	μ
WFS-250-B-1	35,768.45	389	0.017	489.740	0.044	416.28	0.055	0.037	3.164
WFS-250-B-2	35,826.66	378	0.015	484.583	0.044	411.89	0.054	0.038	3.456
WFS-250-B-3	35,875.24	381	0.015	477.993	0.044	406.30	0.056	0.041	3.751
WFS-250-B-4	35,923.59	379	0.015	482.707	0.044	410.29	0.058	0.043	3.891
WFS-250-B-5	35,973.79	393	0.017	487.599	0.044	414.46	0.055	0.038	3.255
WFS-250-B-6	36,022.17	396	0.017	491.550	0.044	417.82	0.055	0.038	3.235
UW-250	33,086.98	356	0.017	434.696	0.044	369.49	0.054	0.036	3.167

The skeleton curve, with rotation (θ) in radians on the *X*-axis and moment (M) in kilonewton-meters (kN·m) on the *Y*-axis, illustrates the bending behavior of the joints under cyclic loading. Initially, the curves are linear, reflecting the elastic stage where the moment increases proportionally with rotation. As loading progresses, the joints transition to a plastic stage, with nonlinear growth eventually reaching a peak moment, representing maximum bending capacity. After the peak, the moment stabilizes or decreases, indicating stiffness degradation as the joints approach failure. The different specimens (WFS-250-B-1, WFS-250-B-2, etc.) show consistent performance, with minor variations in peak moments and stiffness likely due to differences in configuration or testing conditions. Overall, the WFS-250-B joints exhibit good ductility, plastic rotation capacity, and energy dissipation under cyclic loading, with small divergences in their ability to resist repeated loading and seismic performance.

Comparing the performance indices of the UW-250 specimen, it is clear that when l_b/h_b ranges from 0.36 to 0.39 (corresponding to specimens WFS-250-B-3 and WFS-250-B-4), the joint demonstrates excellent plastic rotation capacity and seismic performance.

5.3. WFS-250-C Series Joints

5.3.1. Joint Failure Mode

Figure 16 depicts the PEEQ distribution at failure for the WFS-250-B series joints. Figure 17 presents the curve of the maximum PEEQ at the plastic hinge as a function of loading displacement for the same series.

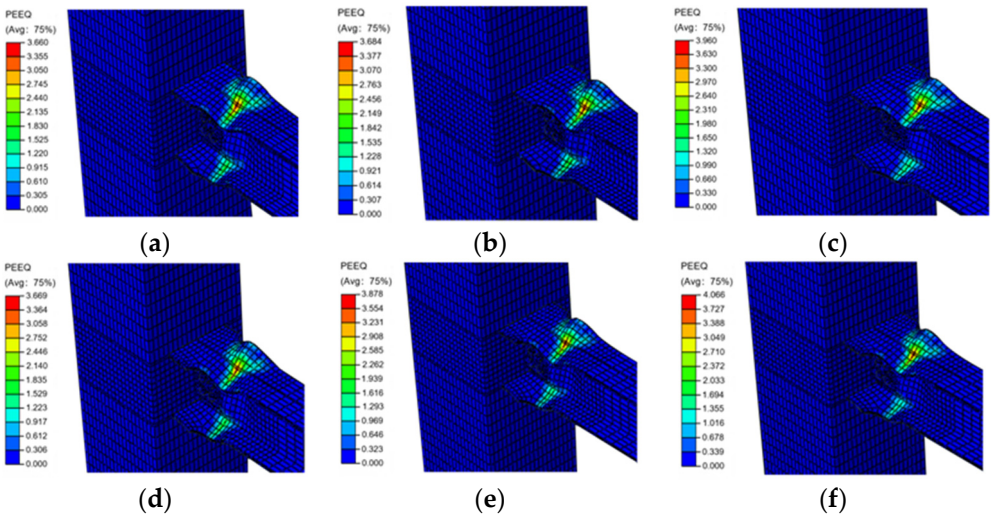

Figure 16. PEEQ cloud chart of WFS-250-C series joints at failure time. (**a**) WFS-250-C-1; (**b**) WFS-250-C-2; (**c**) WFS-250-C-3; (**d**) WFS-250-C-4; (**e**) WFS-250-C-5; (**f**) WFS-250-C-6.

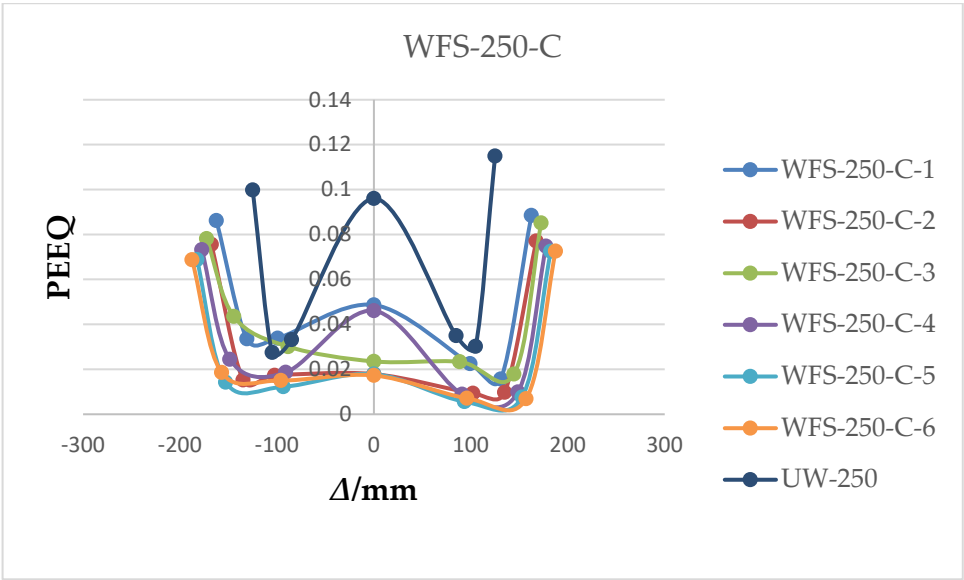

Figure 17. PEEQ maximum at the plastic hinge of WFS-250-C series and UW-250 joints.

Compared to Figures 10 and 13, Figure 16 shows that the failure mode of the WFS-250-C series joints is consistent with that of the WFS-250-A and WFS-250-B series. The upper and lower flanges of the beam buckle form a plastic hinge at the end of the expanded flange. The PEEQ value of the bolt weld between the beam and column flanges gradually decreases while the joint domain remains in the elastic stage with no significant deformation, characteristic of a 'strong joint'. As b_{wf} increases, the plastic deformation decreases, the plastic hinge shifts outward, and the equivalent plastic strain in the beam web outside the connecting plate increases significantly.

The WFS-250-C series introduces an even wider flange section (b_{wf}), greatly influencing the joint's failure mode. The increased width allows for better distribution of plastic deformation across the flanges, further shifting the plastic hinge away from the critical weld zone. This design feature helps reduce the stress concentration at the weld, improving the joint's performance in terms of energy dissipation.

However, the wider flanges experience higher strain at their outer edges, leading to localized buckling as cyclic deformation progresses. The increased flange width also places additional stress on the beam web, making it vulnerable to buckling and other forms

of local deformation. Under continued cyclic loading, the interaction between the wider flanges and the beam web leads to a complex failure mode where both the flanges and the web contribute to the overall failure.

The primary cause of failure in the WFS-250-C series is the combined effect of flange buckling and web deformation. While the widened flange section enhances energy dissipation, it also introduces new failure mechanisms that compromise the joint's long-term seismic performance.

Figure 17 illustrates that for model UW-250, peak PEEQ values were observed at the extreme edges of the beam flange groove weld. When a widened flange was used, the maximum PEEQ index decreased by 23% for WFS-250-C-1 (from 0.115 to 0.088) and 36.9% for WFS-250-C-5 (from 0.115 to 0.073) compared to UW-250. A wider flange at the beam–column interface reduces the PEEQ index. Additionally, Figure 16 shows that WFS-250-C-1 has the highest maximum PEEQ at the plastic hinge, indicating the greatest accumulated plastic deformation, while WFS-250-C-5 has the least. As b_{wf} increases, the plastic hinge's outward displacement increases, and the maximum PEEQ value first increases and then decreases, indicating that the scalar value of cumulative plastic deformation at the plastic hinge follows the same trend.

5.3.2. M–θ Hysteresis Curve and Skeleton Curve

Figure 18 presents the moment-angle M−θ hysteretic and skeleton curves for the WFS-250-C series joints.

Figure 18a shows that the moment-angle M−θ hysteretic curves for the WFS-250-C series joints are all fully shuttle-shaped, exhibiting bearing capacity and energy dissipation. Increasing the width of the reinforced section b_{wf} from 0.15 to 0.25 times the beam width maintains good seismic performance. When the inter-story drift angle reaches 0.06 rad, the joint's bending capacity exceeds 0.85 Mp, similar to the WFS-250-A and WFS-250-B series joints.

The M–θ hysteresis curve shows the relationship between moment (M) in kilonewton-meters (kN·m) and rotation (θ) in radians, reflecting the angular deformation experienced by the structural elements under cyclic loading. The loops in the curve represent energy dissipation, with larger and more spread-out loops indicating greater resilience to repeated loading cycles. Different labels (WFS-250-C-1, WFS-250-C-2, etc.) correspond to various test specimens or conditions. The curve demonstrates a gradual increase in rotation as the moment increases during the loading cycle, followed by a return during unloading, forming hysteresis loops. The overlapping nature of the curves suggests similar performance between the specimens, though some divergence at larger rotations indicates varying degrees of energy dissipation, ductility, or stiffness degradation among the different specimens.

Figure 18b shows that the skeleton curves for all six joints follow the same trend during displacement loading. In the elastic stage, the skeleton curves are nearly straight and coincide with the bending moment, increasing linearly with the rotation angle. After the elastic–plastic stage, nonlinear growth begins, and once the bending capacity peaks, the curves gradually diverge as the joints approach failure, with WFS-250-C-6 exhibiting the fastest decline.

The skeleton curve, with rotation (θ) in radians on the *X*-axis and moment (M) in kilonewton-meters (kN·m) on the *Y*-axis, is derived by connecting the peak points of each cycle from the M–θ hysteresis loops, providing insights into the system's strength, stiffness, and ductility. After a certain rotation, the moment peaks and either stabilizes or decreases slightly, indicating stiffness degradation. The curves for the different specimens show similar trends, indicating consistent performance with only minor variations in peak moments or stiffness, likely due to testing conditions or structural configurations. The hysteresis and skeleton curves reveal crucial information about energy dissipation and stiffness degradation, with some divergence at higher loads, suggesting differences in the ability of the specimens to sustain loads and resist damage under repeated cycles.

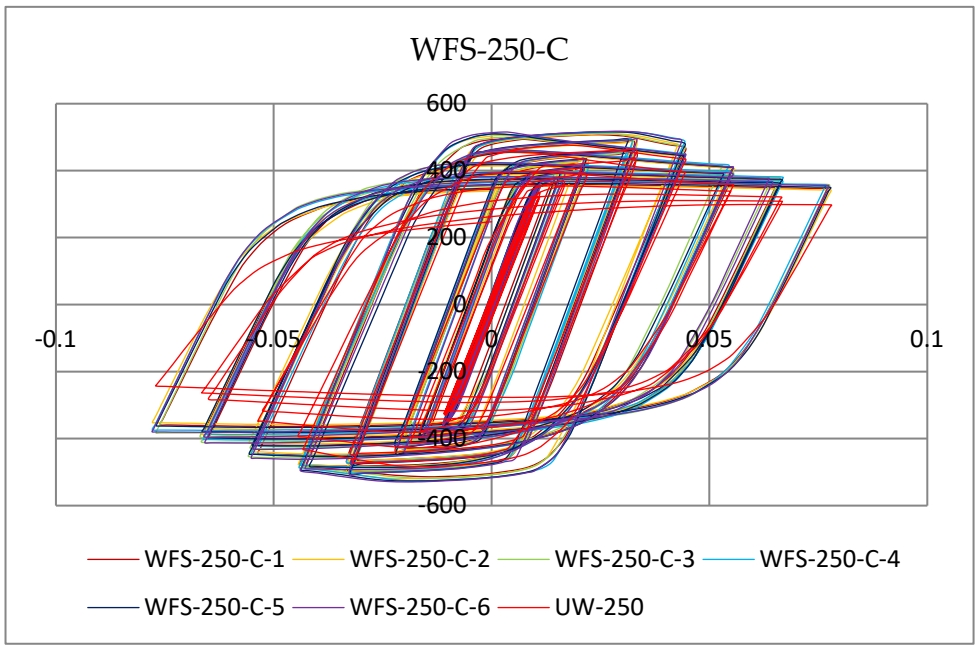

(**a**)

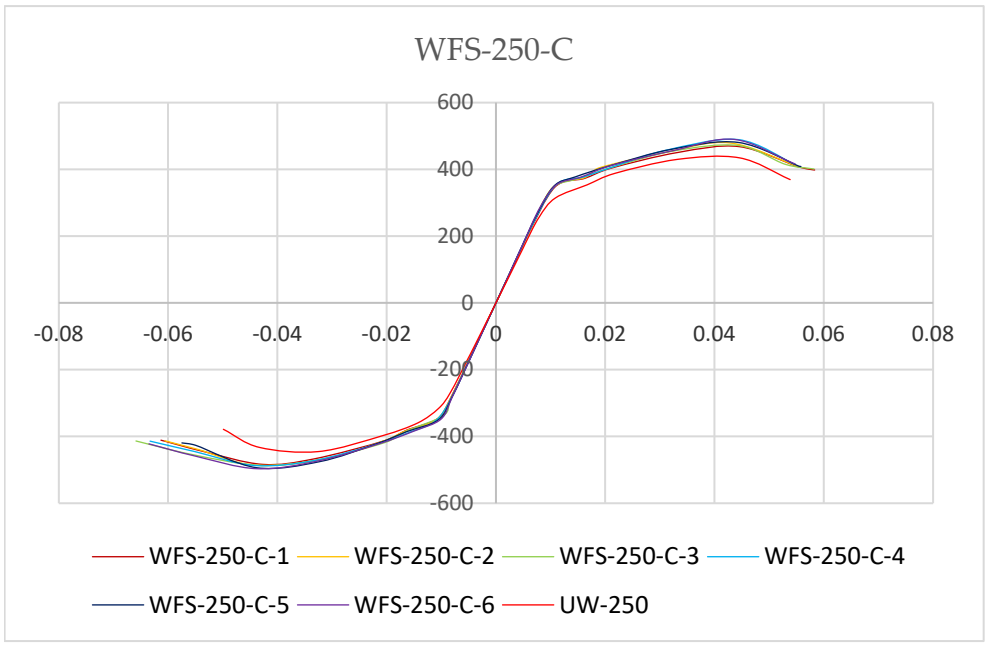

(**b**)

Figure 18. M–θ hysteretic and skeleton curve of WFS-250-B series joints. (**a**) Hysteretic curves; (**b**) Skeleton curves.

Additionally, according to the M–θ skeleton curve of the WFS-250-C series joint in Figure 18b, the joint's mechanical property index when the loading direction is pushing is obtained, as shown in Table 5. The data indicate that increasing the width b_{wf} of the reinforced section increases the yield moment and maximum moment of the WFS-250-C series joints by up to 5.4% and 4.4%, respectively. This suggests that increasing the width of the expanded flange's reinforced section enhances the joint's bending capacity. The yield angle of each joint decreases slightly, while changes in the ultimate angle are minimal, and corner ductility remains similar across the joints.

Table 5. Mechanical performance indexes of WFS-250-C series joints.

Joint Number	R_{ki} /kN·m·rad^{-1}	M_y /kN·m	θ_y /rad	M_{max} /kN·m	θ_{max} /rad	M_u /kN·m	θ_u /rad	θ_p /rad	μ
WFS-250-C-1	34,915.13	370	0.0155	468.151	0.044	397.93	0.055	0.037	3.548
WFS-250-C-2	35,118.17	387	0.0163	479.200	0.043	407.32	0.056	0.038	3.436
WFS-250-C-3	35,300.88	373	0.0150	471.675	0.044	400.92	0.058	0.043	3.881
WFS-250-C-4	35,469.80	391	0.0152	489.144	0.044	415.77	0.055	0.042	3.618
WFS-250-C-5	35,618.35	382	0.0150	480.783	0.044	408.67	0.056	0.041	3.720
WFS-250-C-6	35,768.45	389	0.0173	489.740	0.044	416.28	0.055	0.037	3.164
UW-250	33,086.98	356	0.017	434.696	0.044	369.49	0.054	0.036	3.167

By comparing the performance indices of the UW-250 specimen, it is evident that when b_{wf}/b_f ranges from 0.19 to 0.23 (corresponding to specimens WFS-250-C-3 to WFS-250-C-5), the joint exhibits excellent plastic rotation capacity and seismic performance. This finding aligns with studies on beam–column connections, such as those by Xiao et al. [15] and Han et al. [6], who observed that optimized flange dimensions contribute significantly to energy dissipation and plastic hinge relocation. However, unlike previous research primarily focused on I-section columns and narrow-flange beams, this study extends the understanding to mid-flange H-beams and box columns, revealing that the widened flange connection can further reduce stress concentration and improve cyclic performance under seismic loads.

Furthermore, this research introduces a novel approach to balancing stiffness and ductility in joint design, contrasting with material-based improvements emphasized in prior studies like Yang et al. [7]. While earlier efforts, such as those by Wang et al. [9], focused on enhancing materials like ultra-high-performance concrete, this study prioritizes geometric optimization as a more cost-effective and practical solution.

5.4. Discussion

In summary, the WFS-250 series shifts the focus from material improvements to geometric optimization, offering a streamlined and economical approach to enhancing the seismic performance of steel structures.

These findings align with previous studies by Xiao et al. [15] and Han et al. [6], demonstrating that optimized flange dimensions enhance energy dissipation and aid in plastic hinge relocation. However, this study extends these insights to mid-flange H-beams and box columns, revealing that widened flange connections can reduce stress concentrations and improve cyclic performance under seismic loads.

Additionally, this research introduces a novel approach to balancing stiffness and ductility through geometric optimization, contrasting with earlier studies that emphasized material-based improvements, such as those by Yang et al. [7] and Wang et al. [9], who focused on enhancements like ultra-high-performance concrete. By prioritizing geometric adjustments over material enhancements, this work provides a more cost-effective and practical solution for improving seismic resilience.

6. Conclusions

This study bridges a significant gap in understanding the seismic performance of beam-to-column connections, specifically those involving box columns and mid-flange H-beams. The research demonstrates that incorporating widened beam-end flanges can substantially improve bending capacity and ductility by effectively relocating the plastic hinge away from the connection—an essential factor for enhancing seismic resilience. Key findings from the detailed analysis of failure mechanisms, hysteretic behavior, and mechanical properties are as follows:

1. Performance Comparison: Connections featuring widened flanges outperform traditional H-beam connections with unmodified ends and box columns. The widened

flanges exhibit superior bearing capacity, enhanced seismic performance, and increased ductility, highlighting their effectiveness in improving joint resilience under seismic loads.

2. Flange Length Recommendations: The optimal length for widened beam-end flanges (l_a) ranges from 0.55 to 0.75 times the beam flange width (b_f). This range ensures that the connection benefits from increased moment capacity and energy dissipation without compromising joint performance.
3. Beam Flange Cutting Length: For effective performance, the beam flange cutting length (l_b) should be between 0.36 and 0.39 times the beam depth (h_b). This range balances the need for adequate plastic hinge formation with the structural integrity of the connection.
4. Flange Cutting Depth: The recommended depth for beam flange cutting (b_{wf}) is between 0.19 and 0.23 times the beam flange width (b_f). Adhering to this range optimizes the balance between enhancing ductility and maintaining the structural strength of the connection.

Author Contributions: Conceptualization, L.L.; software, T.D.G.; validation, T.D.G.; resources, L.L.; writing—original draft preparation, T.D.G. and L.L.; writing—review and editing, L.L.; project administration, L.L.; funding acquisition, L.L. All authors have read and agreed to the published version of the manuscript.

Funding: This research was funded by the Nature Science Foundation of China (NSFC), grant number 51278061.

Data Availability Statement: The original contributions presented in the study are included in the article, further inquiries can be directed to the corresponding author.

Conflicts of Interest: The authors declare no conflict of interest.

References

1. Peng, Y. The application and research progress of steel structures in construction industrialization. *IOP Conf. Ser. Earth Environ. Sci.* **2019**, *330*, 022003. [CrossRef]
2. Song, Z.; Gu, Q.; Guo, B. Experimental research on the connection between beam and column of rigid steel frame. *J. Build. Struct.* **2001**, *22*, 53–57.
3. Nakashima, M.; Inoue, K.; Tada, M. Classification of damage to steel buildings observed in the 1995 Hyogoken-Nanbu earthquake. *Eng. Struct.* **1998**, *20*, 271–281. [CrossRef]
4. Mahin, S.A. Lessons from damage to steel buildings during the Northridge earthquake. *Eng. Struct.* **1998**, *20*, 261–270. [CrossRef]
5. Gates, W.E.; Morden, M. Professional structural engineering experience related to welded steel moment frames following the Northridge earthquake. *Struct. Des. Tall Build.* **1996**, *5*, 29–44. [CrossRef]
6. Han, W.; Nie, S.; Chen, Z.; Yang, B.; Deng, Y.; Elchalakani, M. Seismic behavior of high-performance steel (HPS) weakened beam-column joints: Experimental tests and numerical analysis. *J. Build. Eng.* **2024**, *92*, 109807. [CrossRef]
7. Yang, Z.M.; Chen, J.; Wang, F.; Wang, J. Seismic performance of circular concrete-filled steel tube columns reinforced with inner latticed steel angles. *J. Constr. Steel Res.* **2023**, *205*, 107908. [CrossRef]
8. Wei, J.; Ying, H.; Yang, Y.; Zhang, W.; Yuan, H.; Zhou, J. Seismic performance of concrete-filled steel tubular composite columns with ultra high performance concrete plates. *Eng. Struct.* **2023**, *278*, 115500. [CrossRef]
9. Wang, W.Z.; Chen, F.Y.; Huang, Y.Q.; Wang, X.T. Fracture mechanism of joint of H-style steel beam-square steel tubular column and study on joints with horizontal haunch and slot holes at beam flanges. *Eng. Mech.* **2013**, *30*, 197–204.
10. Saneei Nia, Z.; Mazroi, A.; Ghassemieh, M.; Pezeshki, H. Seismic performance and comparison of three different I beam to box column joints. *Earthq. Eng. Eng. Vib.* **2014**, *13*, 717–729. [CrossRef]
11. Lu, L.; Xu, Y.; Zheng, H. Investigation of composite action on seismic performance of weak-axis column bending connections. *J. Constr. Steel Res.* **2017**, *129*, 286–300. [CrossRef]
12. Ma, H.; Wang, J.; Lui, E.M.; Wan, Z.; Wang, K. Experimental study of the behavior of beam-column connections with expanded beam flanges. *Steel Compos. Struct.* **2019**, *31*, 319–327.
13. Wang, M.; Ke, X. Seismic design of widening flange connection with fuses based on energy dissipation. *J. Constr. Steel Res.* **2020**, *170*, 106076. [CrossRef]
14. Zohdi, A.; Matinpour, M.H.; Rafati Bonab, R.; Kiumarsi Oskuei, F. Seismic performance of the enlarged beam section connection. *Steel Constr.* **2024**, *17*, 29–43. [CrossRef]
15. Xiao, Y.; Yu, M.; Liu, W. Finite Element Analysis of Prefabricated Semi-Rigid Concrete Beam–Column Joint with Steel Connections. *Appl. Sci.* **2024**, *14*, 5070. [CrossRef]

16. Wang, Y.; Gao, P. Low-cycle Cyclic Load Test Research on Expanded Joints of Beam End Flanges in Steel Frames. *Build. Struct.* **2010**, *31*, 94–101.
17. *JGJ99-2015*; Technical Specification for Steel Structures of Tall Buildings. China Architecture & Building Press: Beijing, China, 2015.
18. Lu, L.; Zhu, P.; Ding, S.; Ma, Z.; Li, R.; Nie, S.; Wang, W.; Raftery, G.M. Impact of anti-corrosion coatings and maintenance on high-strength bolt friction connections in C4 marine environment. *Structures* **2024**, *68*, 107098. [CrossRef]
19. *JGJ 82-2011*; Technical Specification for High Strength Bolt Connections of Steel Structures. China Architecture & Building Press: Beijing, China, 2011.
20. Nie, W.; Lu, L.; Li, R.; Hao, H.; Luo, T. Global buckling investigation of T-shaped built-up columns composed of two hot-rolled H-shapes. *Structures* **2023**, *58*, 105485. [CrossRef]
21. Kontolati, K.; Apostolos, K.; Olympia, P. Numerical investigation of weak axis I profile connections. In Proceedings of the 9th Hellenic National Conference on Steel Structures, Larissa, Thessaly, Greece, 5–7 October 2017.
22. Gao, P. Experimental Evaluation on the Behavor of Side-Plate Reinforced Section and Widen Flange Section of Steel Frame. Master's Thesis, Qingdao University of Technology, Qingdao, China, 2009.
23. *ANSI/AISC 341-05*; Seismic Provisions for Structural Steel Buildings. American Institute of Steel Construction: Chicago, IL, USA, 2005.
24. Chen, C.C.; Lin, C.C.; Lin, C.H. Ductile moment connections used in steel column-tree moment-resisting frames. *J. Constr. Steel Res.* **2006**, *62*, 793–801. [CrossRef]
25. Chen, C.C.; Lin, C.C.; Tsai, C.L. Evaluation of reinforced connections between steel beams and box columns. *Eng. Struct.* **2004**, *26*, 1889–1904. [CrossRef]
26. *FEMA-350*; Recommended Seismic Design Criteria for New Steel Moment-Frame Buildings. FEMA: Washington, DC, USA, 2000.